Journal of the European Ceramic Society 43 (2023) 5548–5556

Contents lists available at ScienceDirect

Journal of the European Ceramic Society

journal homepage: www.elsevier.com/locate/jeurceramsoc

Lithium mobility along conduction channels of ceramic $LiTa_2PO_8$

K. Kwatek [a,*], W. Ślubowska-Walkusz [a], E. Kwiatkowska [a], J.L. Nowiński [a], A.T. Krawczyńska [b], I. Sobrados [c], V. Diez-Gómez [c], J. Sanz [c]

[a] Warsaw University of Technology, Faculty of Physics, 00–662 Warsaw, Poland
[b] Warsaw University of Technology, Faculty of Materials Science and Engineering, 02–507 Warsaw, Poland
[c] National Research Council, The Materials Science Institute of Madrid (ICMM CSIC), 28049 Madrid, Spain

ARTICLE INFO

Keywords:
Ceramic
Solid electrolyte
Li-ion conductor
Structural features of $LiTa_2PO_8$

ABSTRACT

In the next generation of lithium-ion batteries, the liquid electrolyte is considered to be replaced by its solid counterpart. Recently, a novel Li-ion conductor based on metal oxides emerged – $LiTa_2PO_8$. Due to the high value of bulk conductivity of ca. 10^{-3} S•cm^{-1}, it is believed to be a potential candidate for application as a solid electrolyte in all-solid-state battery technology. In this work, we investigate $LiTa_2PO_8$ ceramics synthesized by a conventional solid-state reaction method with an excess of the lithium-containing substrate to compensate for the loss of Li^+ during sintering. The properties of $LiTa_2PO_8$ ceramics were studied using X-ray diffractometry (XRD), ^{6}Li and ^{31}P magic angle spinning nuclear magnetic resonance spectroscopy (MAS NMR), thermogravimetry (TG), scanning electron microscopy with energy dispersive spectroscopy (SEM/EDS), impedance spectroscopy (IS), DC potentiostatic polarization technique and density method. Referring to the experimental results, increasing of the Li^+ content above the stoichiometric one lowers the total ionic conductivity. The reasons for the deterioration and correlations between microstructure, phase composition, and ionic conductivity are presented and discussed. The MAS NMR spectroscopy has been used to explain high bulk ionic conductivity of $LiTa_2PO_8$ ceramics. A maximum value of total ionic conductivity, 4.5×10^{-4} S•cm^{-1}, was obtained at room temperature for the sample without any excess of Li^+ source.

1. Introduction

In recent years, much research has focused on new functional materials for Li-ion batteries as its improvement is of great importance for industries such as transportation, grid energy and portable electronics [1]. Today, the safety concerns related to electrolytes are one of the crucial issues limiting the range of applicability of lithium-ion batteries. Liquid electrolytes, i.e. lithium salts in mixtures of organic solvents, are used because of their high ionic conductivity. Although performant, they also posses many disadvantages such as flammability, toxicity, and instability in contact with moisture and air. Therefore, there is a growing interest in replacing of liquid electrolytes with their solid counterparts [2–6].

It is generally accepted that a solid electrolyte for commercial application should exhibit a high value of ionic conductivity (at least 10^{-4} S•cm^{-1} at room temperature) as well as a wide electrochemical window and negligible electronic component of total conductivity [3,6,7]. Moreover, it must possess good thermal and mechanical properties, and be chemically stable against lithium, water, and air. It should also be relatively easy to produce on a large scale, cost-efficient, and environmentally friendly. Only a few inorganic solid lithium-ion conductors can meet the criteria mentioned above. Among them, sulphide glasses based on Li_2S in GeS_2-Li_2S-LiI glass-forming system [8,9] can exhibit the ionic conductivity as high as 10^{-3} S•cm^{-1} at room temperature. Despite those encouraging results, the sulphur-based glasses are highly hygroscopic which strongly limits their practical use. Some metal oxide-based compounds have also been investigated as potential solid electrolytes, e.g. perovskite-type $Li_{3x}La_{2/3-x}TiO_3$ (LLTO) [10–12], garnet-type $Li_7La_3Zr_2O_{12}$ (LLZO) [13–15], NASICON-type phosphates $Li_{1+x}Al_xTi_{2-x}(PO_4)_3$ (LATP) [16–21], LISICON-type [22,23] or anti-perovskites $Li_{2+x}OH_{1-x}Cl$ [24,25]. Although they are more chemically stable than sulphide glasses, their total ionic conductivity is still too low for application. Therefore, further research is needed to obtain better conducting, stable solid electrolytes.

Recently, a novel oxide-based solid lithium-ion conductor has emerged, lithium tantalum phosphate $LiTa_2PO_8$ (LTPO) [26–31]. The

---

* Corresponding author.
E-mail address: konrad.kwatek@pw.edu.pl (K. Kwatek).

https://doi.org/10.1016/j.jeurceramsoc.2023.05.013
Received 11 April 2023; Accepted 8 May 2023
Available online 11 May 2023

structure of $LiTa_2PO_8$ is a three-dimensional network of interconnected corner-sharing TaO_6 octahedra and PO_4 tetrahedra. It belongs to a monoclinic system of the C2/c space group. As for electrical properties, experimental studies have demonstrated that ceramic LTPO exhibits a high value of bulk conductivity (10^{-3} S•cm^{-1} at room temperature) [26]. $LiTa_2PO_8$ was also investigated from the theoretical point of view by means of the density functional theory (DFT) and ab initio molecular dynamics (AIMD) simulations [32]. It was reported that the grain conductivity of LTPO may be remarkably high reaching the value of 35.3×10^{-3} S•cm^{-1} at room temperature with an activation energy of 0.16 eV [32]. Those promising predictions have not been confirmed experimentally so far, which suggests that the electrical properties of this compound are not yet at its optimal level.

Similarly to other ceramic Li^+ conductors, LTPO suffers from a deterioration of the total ionic conductivity due to the existence of highly-resistant grain boundaries. Because of that, its total conductivity is about one order of magnitude lower than the grain conductivity [26–31]. In order to understand and possibly overcome this obstacle, some experimental studies have been conducted in recent years. B. Huang et al. [28] showed that some secondary phases appear when the material is sintered at 1075 °C and above, or when the sintering time is longer than 24 h. They explained those results by lithium evaporation at elevated temperatures during prolonged heat-treatment. Regardless of sintering temperature and time, all samples exhibited nearly the same value of the total ionic conductivity of 10^{-4} S•cm^{-1}. Another study by Q. Zhang et al. [29] evidenced that the excess of Li_2O additive resulted in higher relative density of LTPO ceramics and thus in higher total ionic conductivity reaching 3.3×10^{-4} S•cm^{-1} at room temperature. In yet another research, R. Kim et al. [30] managed to dope LTPO material with Si and reached a high value of total ionic conductivity, 1.2×10^{-3} S•cm^{-1} at room temperature for the chemical composition of $Li_{1.4}Ta_2P_{0.6}Si_{0.4}O_8$. The authors concluded that the enhanced electrical properties of the Si-doped LTPO may be ascribed to an increased content of lithium ions that occupy sites close to P/Si atoms.

The reports mentioned above indicate that one of the factors limiting the total conductivity of LTPO ceramics is the loss of lithium ions during high temperature processing. Therefore, it seems justified to assume that the content of lithium exceeding the nominal composition should be beneficial if one intends to improve the ionic conductivity of LTPO. In this work, we propose to synthesize $LiTa_2PO_8$ material by a conventional solid-state reaction method with an excess of the substrate containing Li ions to compensate for the loss of the lithium ions in the ceramics during sintering. The primary purpose of this work is to systematically examine the impact of the technological protocol on the phase formation, microstructure and electrical properties of LTPO. We emphasize the enormous relevance of the microstructure as well as the phase purity of the studied ceramics on high values of the total ionic conductivity. A detailed analysis of the ^6Li and ^{31}P MAS NMR spectra as a function of temperature was finally used to explain high bulk conductivity values of $LiTa_2PO_8$.

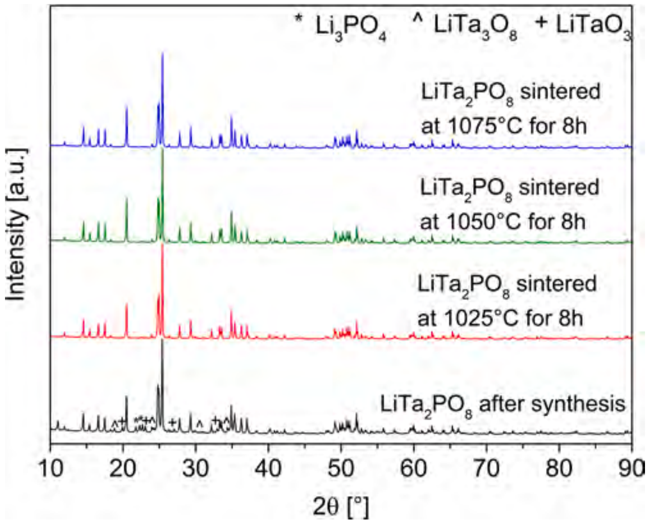

Fig. 1. XRD patterns of $LiTa_2PO_8$ + 0 wt% material obtained after synthesis and after sintering at 1025 °C, 1050 °C or 1075 °C for 8 h.

2. Experimental

Polycrystalline $LiTa_2PO_8$ compound was synthesized by means of a conventional solid-state reaction method with stoichiometric amounts of Li_2CO_3 (Sigma Aldrich), $NH_4H_2PO_4$ (POCh) and Ta_2O_5 (Roth). The 0 wt%, 5 wt%, 10 wt% or 15 wt% excess of lithium source, namely Li_2CO_3, was added to compensate the Li_2O evaporation due to heat treatment at high temperatures. The weighted chemicals were mixed in ethanol as an immersion liquid at 300 rpm for 20 h using Fritsch Pulverisette 7 Classic Line planetary ball mill. The obtained mixture of reagents was dried, placed in a platinum crucible, and first annealed in a muffle furnace at 600 °C for 8 h and then heated at 1000 °C for 8 h. The as-obtained synthesized material was ball milled with ethanol and one droplet of PEG (Sigma Aldrich) for 1 h at 400 rpm in planetary mill Fritsch Pulverisette 7. Then, the powder was pressed under uniaxial 2 MPa pressure to obtain pellets with 6 mm diameter and ca. 2 mm thickness. Then, the pellets were placed in oil press under 400 MPa pressure to ensure good compactness of the material. Eventually, the pellets were sintered at 1025, 1050 or 1075 °C for 8 h in a muffle furnace.

The phase composition of the as-prepared and sintered powders was examined using the X-ray diffraction method. Data were collected in the 2θ range from 10° to 90° with 0.013° step and counting rate of 300 s per step with CuKα line using a Philips X′Pert Pro diffractometer.

The thermal stability of the as-synthesized powders was determined by thermal gravimetric analysis (TGA). A TA Instruments Q600 calorimeter was used to register the mass loss and the temperature difference (with reference to an empty alumina crucible) during heating under airflow in the temperature range from 50° to 1100°C. The measurements were performed at the heating rate of 10 °C.min^{-1} on powdered samples of ca. 20 mg each.

^6Li and ^{31}P MAS NMR spectra were recorded with a Bruker AVANCE-400 spectrometer (9.4 T magnetic field). The frequencies of 58.8 and 161.9 MHz for ^6Li and ^{31}P, were used respectively. The MAS technique, i.e. rotation of samples at 10 kHz around an axis inclined 54°44′ with respect the external magnetic field was applied. MAS NMR spectra were recorded after 2.0 μs irradiation for lithium, 4.0 μs irradiation ($\pi/2$ pulses) for phosphorus. To avoid saturation effects, the recycle delay of 5 s was chosen in the case of ^6Li and the delay of 60 s was used in the case of ^{31}P signals. The spectra were collected with 24 and 800 scans for ^{31}P and ^6Li, respectively. Chemical shift values of NMR resonances were referred to 1 mol.L^{-1} LiCl and 85 wt% H_3PO_4 aqueous solutions. The NMR spectra were simulated using *dmfit* software [33].

The apparent density of the pelletized samples was determined by Archimedes method with isobutanol (Sigma Aldrich) as an immersion liquid. The accuracy of this method was estimated as ca. 1%. To study the microstructure of sintered materials, cross sections of freshly fractured pellets were polished by an ion milling system IM 4000 and subsequently observed using a scanning electron microscope (SEM) SU8000 Hitachi at 5 kV in secondary electron (SE) and backscattered electron (BSE) modes. The electron dispersive X-ray analysis (EDX) was performed at 5 kV. Additionally, a cross-sectional lamella was prepared by focused ion beam (FIB) Hitachi NB5000. Subsequently, its microstructure was observed using transmission electron microscope (TEM) JEOL JEM 1200 at 120 kV.

For impedance spectroscopy measurements, both faces of pellets were polished with sandpaper and covered with Pt electrodes. Impedance investigations were carried out using a Solartron 1260 frequency analyzer in the frequency range from 1 to 10^7 Hz in the temperature

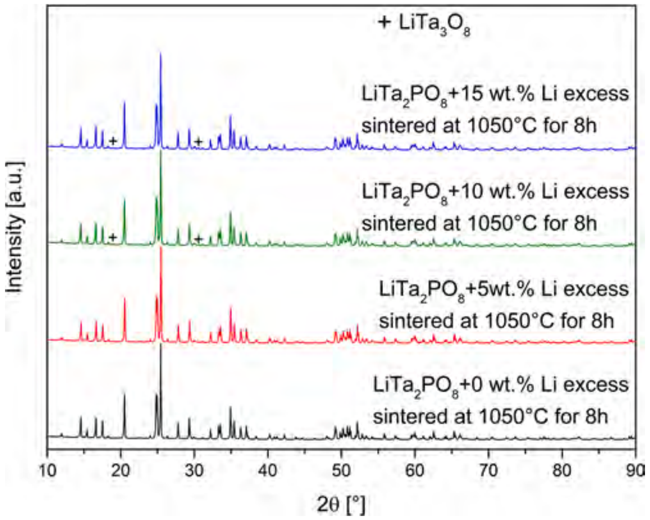

Fig. 2. XRD patterns of the ceramic $LiTa_2PO_8$ materials with different amounts of Li containing substrate after sintering at 1050 °C for 8 h.

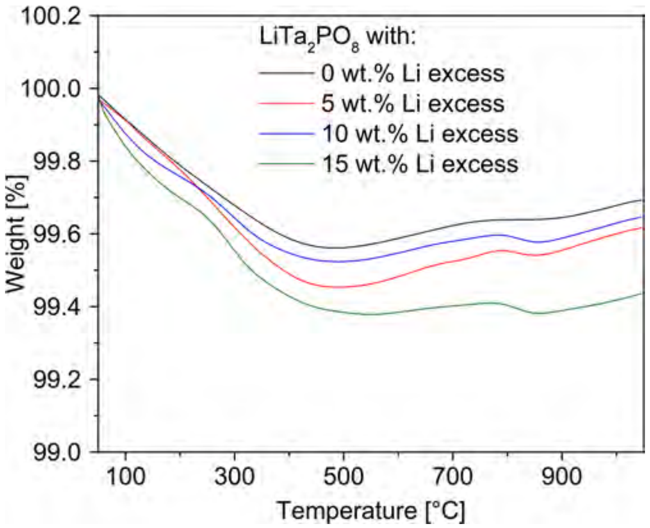

Fig. 3. TG traces for $LiTa_2PO_8$ with different content of excess of Li source.

range from + 30 to + 100 °C, during heating and cooling runs. The impedance data were collected using a self-developed software [34]. DC potentiostatic polarization technique was used to evaluate the electronic conductivity of the ceramics. For this purpose, a constant voltage of 1.0 V was applied to a symmetric Pt/$LiTa_2PO_8$/Pt cell for 36000 s (10 h). The value of the electronic conductivity was computed using the following formula:

$$\sigma = \frac{U}{I}\cdot\frac{d}{S},$$

where U is the constant potential difference applied, I is the current, d is the thickness of the ceramic and S is the area of the electrode.

3. Results and discussion

3.1. X-ray diffraction

Fig. 1 presents X-ray diffraction patterns for as-synthesized and ceramic $LiTa_2PO_8$ materials sintered at 1025, 1050 or 1075 °C for 8 h. In the case of the non-sintered material, the positions and relative intensities of the main reflections correspond to the monoclinic C2/c unit cell (ICDD 04–025–5910). However, besides them, there are also some additional small diffraction peaks assigned to $LiTa_3O_8$ (18.8°, 24.4°, 30.5°, 34.5°), $LiTaO_3$ (19.9°, 23.1°, 27.0°, 32.9°) and Li_3PO_4 (21.8°, 22.3°, 22.7°) phases. The diffraction lines attributed to the secondary phases disappeared when the material was sintered at high temperatures. Moreover, no additional peaks appeared for ceramics, which proves their good phase purity.

In Fig. 2 diffraction patterns for LTPO sintered at 1050 °C for 8 h with different amounts of Li-containing substrate are shown. No secondary phases were observed for the material with 0 wt% and 5 wt% excess of lithium source. However, for the ceramics with 10 wt% and 15 wt% excess of lithium source, two low-intensity diffraction lines belonging to the $LiTa_3O_8$ phase appeared at 18.8 and 30.5°.

3.2. Thermal analysis

Thermogravimetry (TGA) results for the as-prepared LTPO powders are presented in Fig. 3. Regardless of the Li excess value, the most pronounced mass loss of ca. 0.5% always occurs up to 400 °C. It corresponds to the evaporation of moisture and residual ethanol absorbed at grain boundaries. For higher temperatures, around 800 °C, one may discern a small (less than 0.04%) mass loss for materials with 5 wt%, 10 wt% and 15 wt% excess of lithium source, which may be attributed to the formation of secondary phase/phases identified by means of the XRD method.

3.3. MAS NMR

The ^{31}P (I = 1/2) and ^{6}Li (I = 1) MAS NMR spectra were recorded in powdered $LiTa_2PO_8$ ceramics sintered at 1050 °C with 0 wt% and 15 wt % excess of lithium-containing substrate. In the case of P atoms, dipolar P–Li and chemical shift anisotropies are attenuated by the sample rotation around an axis inclined 54°44’ with respect the external magnetic field (MAS NMR technique). As for Li atoms, in addition to dipolar (Li–Li, P–Li) and chemical shift interactions, quadrupolar interactions contribute to the broadening nuclear transitions. In presence of mobile Li^+ ions, above mentioned interactions are further averaged at increasing temperatures.

Fig. 4 presents the ^{31}P MAS NMR spectrum of the $LiTa_2PO_8$ ceramic

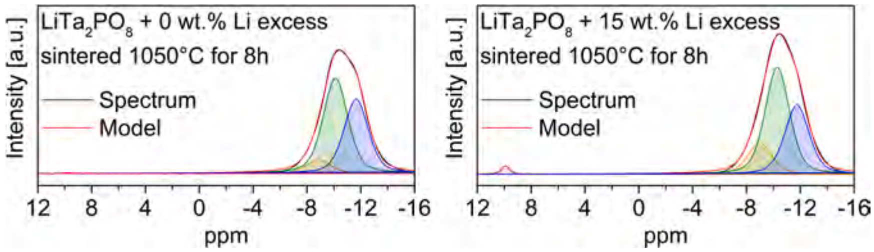

Fig. 4. ^{31}P MAS NMR spectra for LTPO+ 0 wt% and LTPO+ 15 wt% sintered at 1050 °C for 8 h. The experimental and simulated spectra are displayed as black and red lines, respectively. The simulated spectra is the sum of distinct lineshapes shown in colours.

Table 1
Relative integrated intensities (II) in %, full widths at half maximum height (FWHM) in ppm and isotropic chemical shifts (δ) of the lineshapes used to simulate ^{31}P MAS NMR spectra of Fig. 4.

	$LiTa_2PO_8$#1			$LiTa_2PO_8$#2			$LiTa_2PO_8$#3			Li_3PO_4		
Sample	δ [ppm]	FWHM [ppm]	II [%]	δ [ppm]	FWHM [ppm]	II [%]	δ [ppm]	FWHM [ppm]	II [%]	δ [ppm]	FWHM [ppm]	II [%]
LTPO + 0 wt% Li excess	− 8.88	2.14	7.5	− 10.12	2.16	52.2	− 11.66	2.14	40.2	9.90	0.5	0.1
LTPO + 15 wt% Li excess	− 9.00	2.14	15.1	− 10.29	2.14	50.3	− 11.75	2.14	33.2	9.91	0.7	1.4

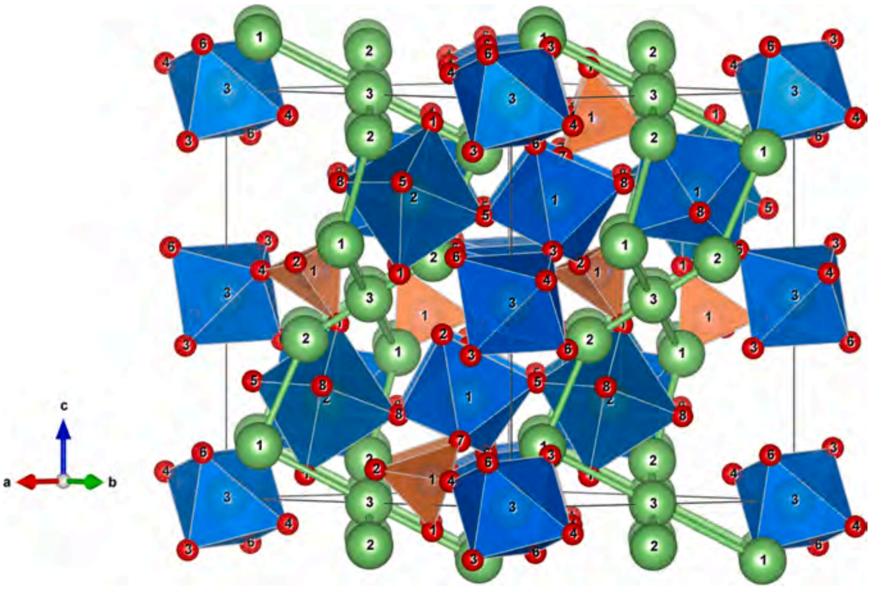

Fig. 5. Crystal structure of $LiTa_2PO_8$ with schematic connection between the Li positions.

sintered at 1050 °C with 0 wt% excess of Li source, mainly dominated by one asymmetric peak at − 10.3 ppm. Due to its asymmetry, the experimental envelope may be deconvoluted into three overlapping signals at: − 8.9, − 10.1, and − 11.7 ppm. For the material with 15 wt% excess of Li substrate (Fig. 4), the shape of the main resonance peak remains nearly the same. The small shift detected toward more negative values was associated with changes on the signal intensity of the − 8.9 and − 11.7 ppm peaks, where the former one increases and the latter one decreases. Moreover, one may observe one additional line at 9.9 ppm assigned to Li_3PO_4 phase [35,36]. More detailed information about the relative integrated intensities and FWHM values may be found in Table 1.

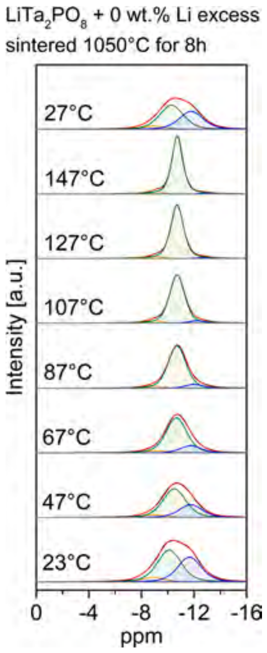

Fig. 6. The variable temperature ^{31}P MAS NMR spectra for LTPO+ 0 wt% sintered at 1050 °C for 8 h. The experimental and simulated spectra are displayed as black and red lines, respectively. The simulated spectra is the sum of distinct lineshapes shown in colours.

To better understand the shape and evolution of NMR spectra, first the $LiTa_2PO_8$ structure should be considered (Fig. 5). Generally, it is built up by three corner-sharing Ta octahedra along three orthogonal directions. In this compound, there exist only one crystallographic site for phosphorus, that share oxygens with four tantalum octahedra to form $P(OTa)_4$ environments [26]. In $LiTa_2PO_8$, Li(3) sites are interconnected by means …Li(3)-Li(1)-Li(2)-Li(3)… or …Li(3)-Li(2)-Li(1)-Li (3)… paths, along conduction channels disposed parallel to the c-axis. The occupation of Li(1), Li(2) and Li(3) sites, reported by J. Kim et al. was 0.72, 0.21 and 0.14 respectively [26].

If one considers the tetrahedral coordination of phosphorus in the $LiTa_2PO_8$ structure (as reported by J. Kim et al. [26]), one may notice that the P–O2 bond (1.47 Å) is slightly shorter than the three other (<P–O> = ~1.54 Å). Moreover, O–P–O angles differ from those of an ideal tetrahedron, i.e. O1–P–O7 angle has the lowest value of 106.7°, while the one for O2–P–O7 is characterized by the highest value of 113.7°. Thus, the ^{31}P coordination in $LiTa_2PO_8$ differs from the ideal tetrahedron in terms of the bond lengths and angles between those bonds. The differences produced in four P–O–Ta bond distances could

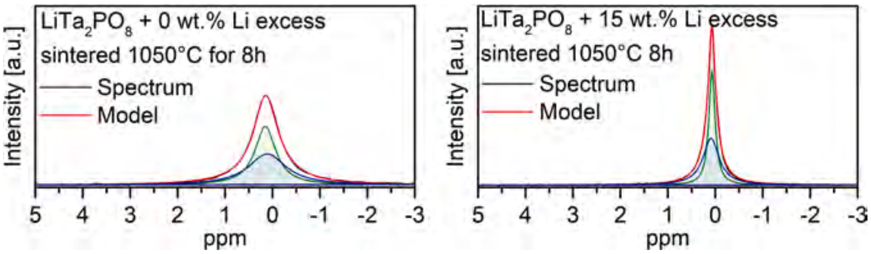

Fig. 7. ^{6}Li MAS NMR spectra for LTPO+ 0 wt% and LTPO+ 15 wt% sintered at 1050 °C for 8 h. The experimental and simulated spectra are displayed as black and red lines, respectively. The simulated spectra are the sum of distinct lineshapes shown in colours.

yield chemical shift anisotropies, that could be related to local symmetry and tetrahedral distortions [37–42]. However, chemical anisotropies deduced from ^{31}P MAS NMR spectra are $\Delta\sigma \sim 35$ ppm and $\eta \sim 0.3$, indicating that tetrahedral distortions should be negligible in this case.

The ^{31}P MAS NMR chemical shift is sensitive to a second-cation neighbours, particularly to the concentration and distribution of Ta and Li ions Assuming that the chemical anisotropy effects are not significant, it is expected that chemical shift differences can be produced by Li cations. In particular, more abundant Li(1) atoms are bonded to O1 and O7 oxygens at 2.0 and 2.2 Å distances. Considering the average occupation of structural sites, phosphorus environments with one or two Li^+ ions should be the most probable. This analysis suggest that phosphorus environments with no lithium ions should be much less probable.

As Li atoms change charges of oxygens bonded to phosphorus atoms, it is possible that three ^{31}P signals in NMR spectra (Fig. 4) may be related to the number of Li^+ ions that share oxygens with PO_4 tetrahedra. Based on these considerations, three detected signals at − 8.9, − 10.1, and − 11.7 ppm could be tentatively ascribed to phosphorus atoms surrounded by zero, one and two Li^+ ions bonded to tetrahedra oxygens. The relative intensities of these components, suggest that most probable environments of ^{31}P are four tantalum ions and one or two Li^+ ions. From this fact, changes in intensities of different signals could be used to track the Li^+ rearrangement along conduction channels in LTPO [37–42].

The ^{31}P MAS NMR experiments for LTPO+ 0 wt%Li excess performed at increasing temperatures showed an increase of the − 10.1 ppm resonance and a decrease of the − 11.7 ppm one, whereas the resonance at − 8.9 ppm remained almost unaffected (see Fig. 6 and Table S1). The increase of temperature facilitates the hopping of Li^+ ions between different sites. That favours the detection of a single averaged component at − 10.7 ppm at increasing temperatures, suggesting that Li(1) and Li(2) ions exchange their positions, causing ^{31}P atoms to interact with one Li^+ atom on average. A decrease of temperature recovers the original spectrum, indicating the reversible allocation of Li ions at structural sites deduced in refinements.

Fig. 7 presents the ^{6}Li (I = 1) MAS NMR spectra of $LiTa_2PO_8$ ceramics sintered at 1050 °C with 0 wt% and 15 wt% amount of the substrate containing Li ions. Due to small dipolar and quadrupolar interactions in the ^{6}Li signal, only central (CT) transitions of ^{6}Li MAS NMR spectra were detected. Generally, in each case, just one peak may be observed at: 0.14 ppm and 0.07 ppm for materials with 0 wt% and 15 wt% of excess of Li substrate, respectively. Deconvolution of the spectra revealed the presence of two components placed close to each other but with different linewidth. The relative integrated intensity of the two major peaks is nearly the same, equal to approximately 50%. Taking into account the relative occupations of Li(1), Li(2), and Li(3) sites in the structural network of $LiTa_2PO_8$ (0.72, 0.21, and 0.14) [26], two detected signals cannot be directly related to the occupation of those sites. On the other hand, NMR spectra suggest the presence of two Li species with different mobility due to detecting two components with different linewidth [43]. The narrow linewidth may be ascribed to Li ions with high mobility, while the broad one with lower mobility. Based on occupancies deduced in previous structural refinements [26], we have ascribed the narrow Li NMR component to Li(1) or Li(2) ions exchanging their structural positions in P environments with two Li^+ ions. On the other hand, the broad component has been ascribed to Li^+ ions in P environments with only one Li^+ ion. A simple estimation of two Li species would be 0.42 (Li(1) + Li(2) pairs) and 0.51 (isolated Li(1) ions), which is not far from experimental observations.

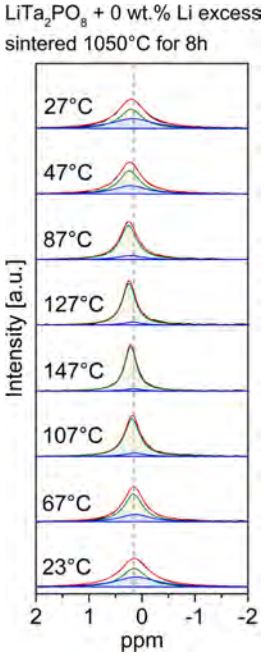

Fig. 8. The variable temperature ^{6}Li MAS NMR spectra for LTPO+ 0 wt% sintered at 1050 °C for 8 h. The experimental and simulated spectra are displayed as black and red lines, respectively. The simulated spectra is the sum of distinct lineshapes shown in colours.

At increasing temperatures (see Fig. 8 and Table S2), isolated Li(1) ions participate in exchanges with other Li^+ ions (Li(1) and Li(2) of neighboring segments), making that only one averaged environment may be detected in ^{31}P MAS NMR spectra. In this case, the averaged environment requires that mobile Li^+ ions also occupy Li(3) sites, making Li^+ ions reside at different times at three detected sites. This assignment explains ^{31}P MAS NMR results, where two main detected components merge in a single one when extended motions are produced. At room temperature, local motions are produced, but above 100ºC, extended motions are dominant. In agreement with this idea, DC conductivity increases considerably with temperature. The low occupancy of Li(3) sites ensures the onset of essential mobility of lithium at moderate temperatures in $LiTa_2PO_8$.

3.4. Microstructure and apparent density

The SEM images taken in the BSE and SE modes for the $LiTa_2PO_8$

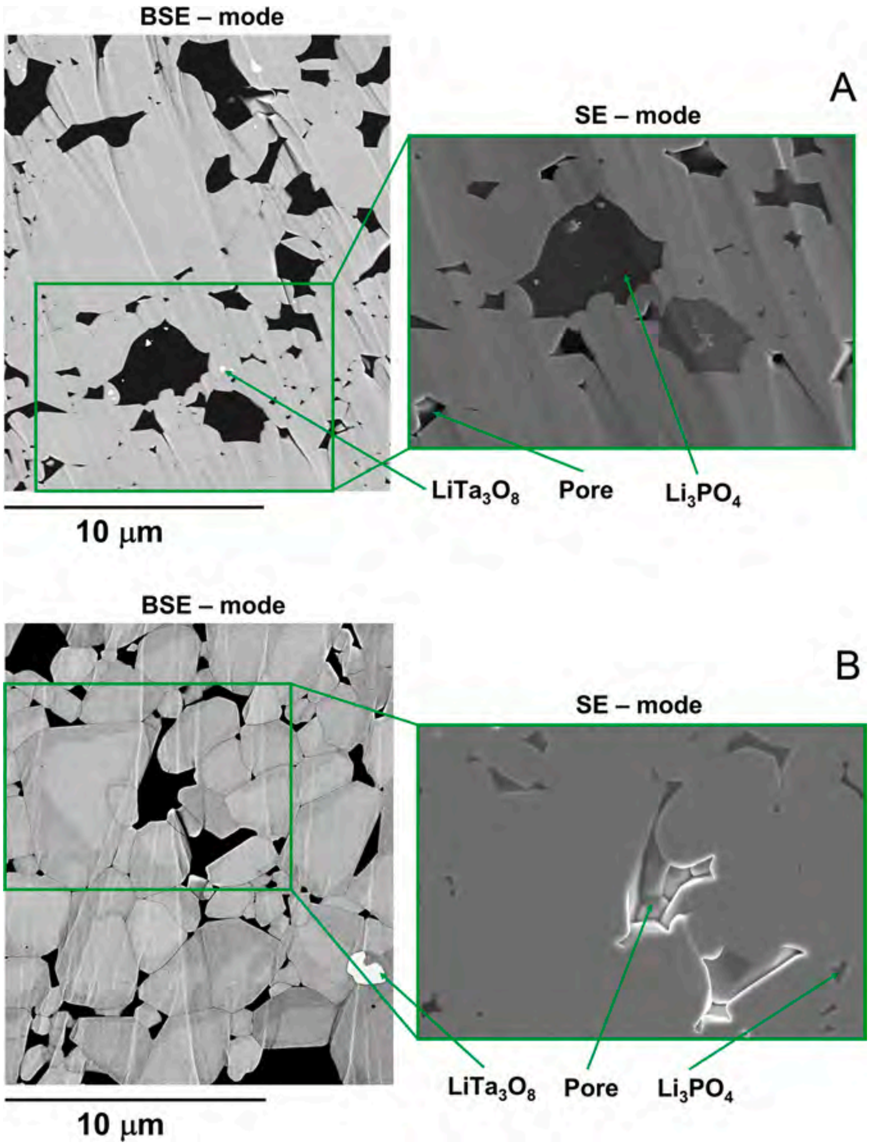

Fig. 9. SEM images of the LTPO+ 0 wt% (A) and LTPO+ 15 wt% (B) ceramics sintered at 1050 °C for 8 h taken in SE or BSE modes.

ceramic sintered at 1050 °C for 8 h with 0 wt% (Fig. 9 A) and 15 wt% (Fig. 9B) excess of lithium source were analysed. For material with 0 wt % excess of lithium source, the microstructure exhibits an inhomogeneous grain size distribution. In micrographs, mainly small grains are discernible (ca. 1 µm in diameter) along with some medium ones (2.5 µm) and a small amount of bigger ones (ca. 6 µm).

Fig. 9 A also shows some darker areas, which can be correctly analysed only when images taken in BSE and SE modes are compared (inset of Fig. 9 A). Those darker areas may be classified as pores or secondary phases containing light elements. The size of each pore is ca. 2 µm and their concentration is relatively high. One may also notice small white areas (ca. 200 nm in size), representing secondary phase containing heavy elements. The secondary phases were identified using the EDX technique (see Fig. S1 and Table S3). The bright areas contain Ta and O, so they are probably precipitations of the $LiTa_3O_8$ phase, which was already identified by XRD investigations. The darker areas are composed of light elements and do not contain Ta, the element with the highest atomic number. Therefore, based on the EDX and ^{31}P MAS NMR investigations results, we conclude that the darker areas contain: P and O elements and it is probably Li_3PO_4 phase.

The microstructure of the ceramic sintered at 1050 °C for 8 h with 15 wt% excess of lithium source is more compact (Fig. 9B) than in the case of 0 wt% sample. Also, the porosity is lower and the grain size distribution is more uniform, i.e. there is a higher number of larger grains. Such change of microstructure mainly affects the triple boundary regions where three types of grains, irregular in shape and size, adhere. For material with the excess of Li source, it may be observed that the area of triple boundary region is more extensive, which means that the grains do not adhere to each other very well. Additionally, the content of the secondary phases is also different. The white areas in the BSE mode image, ascribed to the $LiTa_3O_8$ phase are more extensive, whereas the areas identified as the Li_3PO_4 phase are smaller, but their concentration is higher. Nevertheless, in both cases, for 0 wt% and 15 wt%, one may find the evidence of secondary phases like $LiTa_3O_8$ or Li_3PO_4, with different concentration.

The TEM images were taken at $LiTa_2PO_8$ sample without excess of lithium source after sintering at 1050 °C for 8 h. At a first glance, two different types of regions may be observed, bright and dark. The latter one, which is the most abundant corresponds to $LiTa_2PO_8$ phase. However, more thorough observation of the microstructure revealed that the darker regions, assigned to LTPO phase may be crystalline or amorphous (see Fig. S2). Moreover, the sample degrades under the ionization effect of the electron beam (Fig. S3), which also has been reported by R. Kim et al. [30]. In the case of the brighter areas, they mainly occur in the

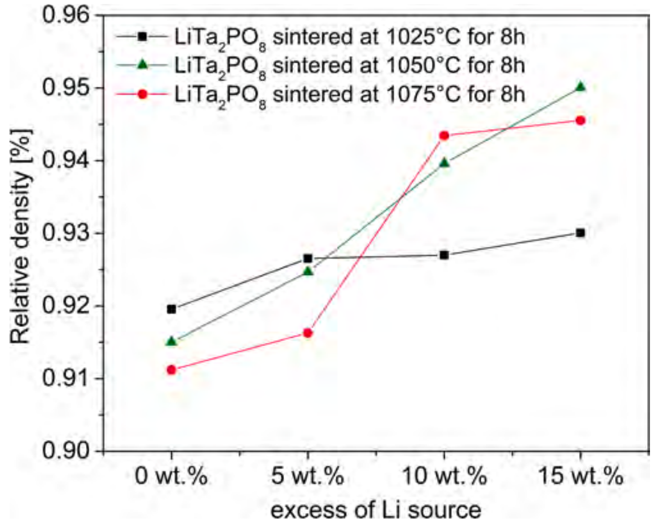

Fig. 10. Relative density values with different excess amount of the substrate containing Li ions sintered at 1025 °C, 1050 °C or 1075 °C for 8 h.

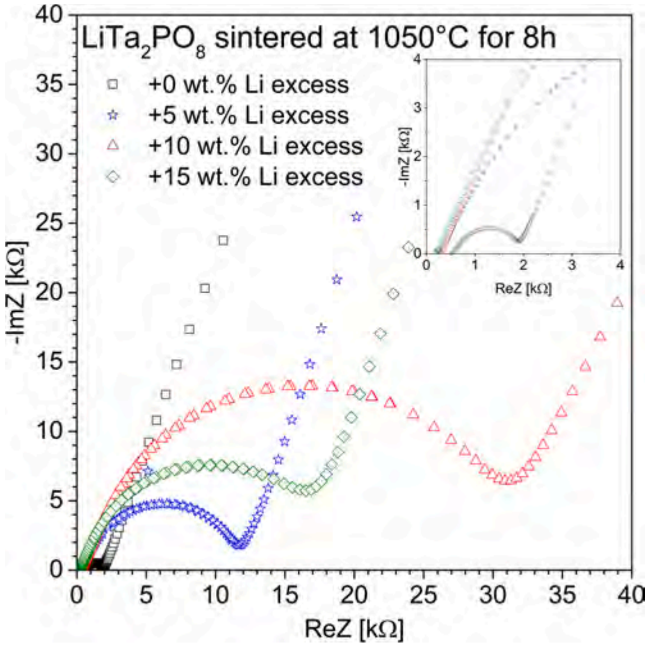

Fig. 11. Nyquist plots for the data collected at 30 °C for $LiTa_2PO_8$ sintered at 1050 °C for 8 h with different content of excess of Li source.

triple boundary regions, but also at grain boundaries (Fig. S3). Referring to the SEM analysis, it may suggest that bright areas present on TEM images correspond to Li_3PO_4 phase, which is formed in the triple boundary regions.

Fig. 10 presents the relative density as a function of Li excess content for $LiTa_2PO_8$ ceramics under study. It can be deduced that the relative density values increase with the excess of lithium source, regardless of the sintering temperature. Although the less pronounced density increase is observed for pellets sintered at the lowest temperature, namely 1025 °C. These results correlate well with the SEM images, where the microstructure is denser for materials with an excess of Li source.

3.5. Impedance spectroscopy

The impedance spectroscopy results are presented in Figs. 11, 12 and 13. The illustrative Nyquist plots collected at 30 °C for $LiTa_2PO_8$

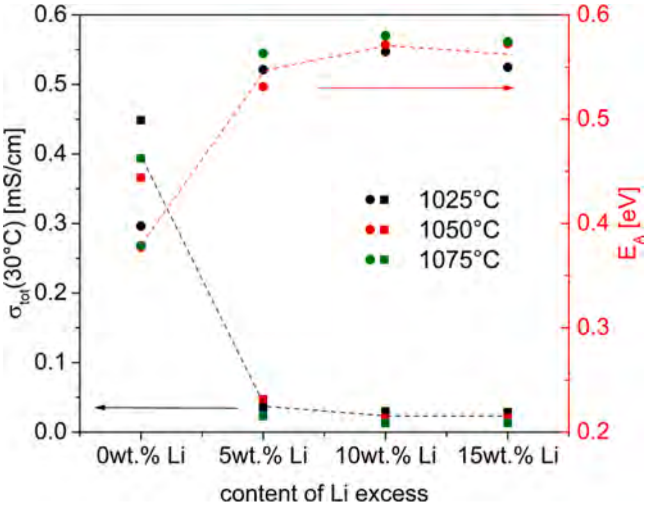

Fig. 12. The values of total ionic conductivity (σ_{tot}) and activation energy (E_A) with different excess amount of the substrate containing Li ions sintered at 1025 °C, 1050 °C or 1075 °C for 8 h.

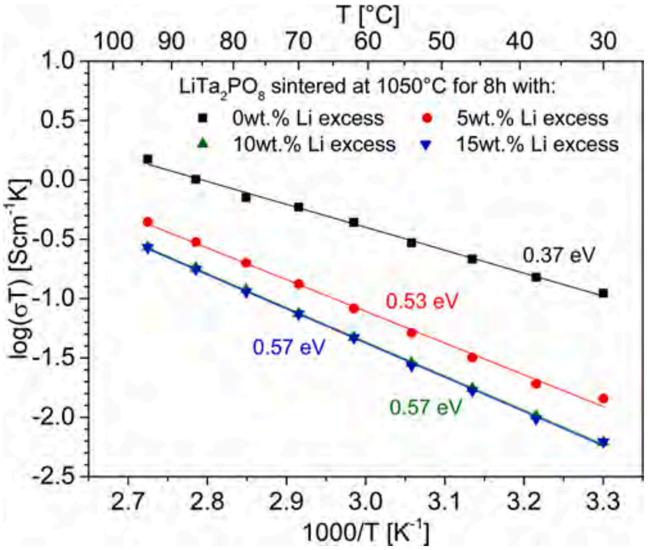

Fig. 13. Arrhenius plots of the total ionic conductivity of the $LiTa_2PO_8$ materials with different amounts of Li containing substrate after sintering at 1050 °C for 8 h.

Table 2
The values of total ionic conductivity and its activation energy for the LTPO ceramics with different excess amount of Li containing substrate.

Sample	T_{sint} [°C]	σ_{tot} (30 °C) [S•cm^{-1}]	E_{tot} [eV]
LTPO + 0 wt% Li excess	1025	4.5×10^{-4}	0.40
	1050	3.7×10^{-4}	0.37
	1075	3.9×10^{-4}	0.38
LTPO + 5 wt% Li excess	1025	3.5×10^{-5}	0.55
	1050	4.8×10^{-5}	0.53
	1075	2.3×10^{-5}	0.56
LTPO + 10 wt% Li excess	1025	3.0×10^{-5}	0.56
	1050	2.0×10^{-5}	0.57
	1075	1.3×10^{-5}	0.58
LTPO + 15 wt% Li excess	1025	2.9×10^{-5}	0.55
	1050	2.0×10^{-5}	0.57
	1075	1.3×10^{-5}	0.57

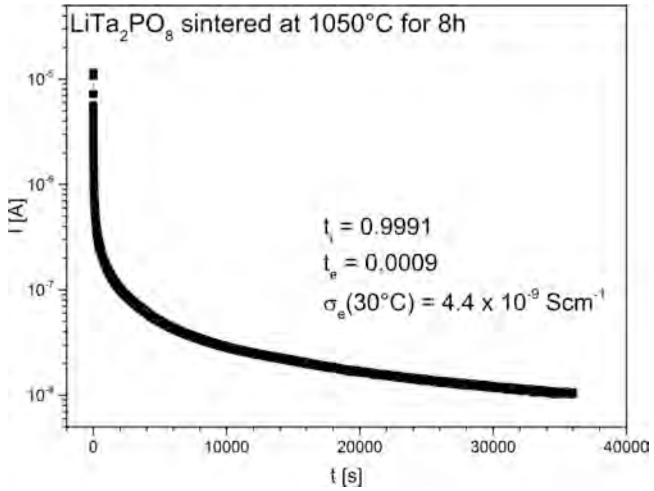

Fig. 14. The DC polarization curve of the $LiTa_2PO_8 + 0$ wt% material sintered at 1050 °C for 8 h.

sintered at 1050 °C for 8 h with different amount of the excess of Li substrate are given on Fig. 11. All of them are characterized by a single, regular semicircle followed by a spur at lower frequencies. The values of the total ionic conductivity may be evaluated using the formula $\sigma = L/(R{\cdot}A)$, where L and A stand for the sample thickness and electrode area, respectively. The total resistance R can be derived from the semicircle intersection with Re Z axis. The estimated values of the total conductivities are given in Table 2 and Fig. 12. One may notice that, regardless of the sintering temperature, the values of the total ionic conductivity are nearly the same for each composition. But, the values of σ_{tot} drop significantly when the excess of Li source is introduced.

The total ionic conductivity as a function of temperature exhibits an Arrhenius-like dependence. The exemplary Arrhenius plots for LTPO ceramics sintered at 1050 °C are presented in Fig. 13. The values of the activation energy and total ionic conductivity are shown in Fig. 12 and Table 2. Ceramics with an excess of Li source are characterized by higher value of the activation energy (0.53–0.57 eV), whereas for samples without Li excess E_a is lower and equal to ca. 0.37 eV. The reason for higher value of E_a in the latter case may be the formation of secondary phases impeding the transport of lithium ions through grain boundary region.

The DC polarization curve is shown in Fig. 14 for the Pt||LTPO||Pt system. The obtained results indicate that $t_i = 0.9991$and the electrical conductivity value, ca. 4×10^{-9} S•cm^{-1} is about 5 orders of magnitude lower than the ionic one and may be neglected.

As for the electrical properties of the LTPO material, one can conclude that increasing the content of Li^+ ions above the stoichiometric one is inefficient to obtain a good ionic conductor. On contrary, this study indicates that an excess of Li ion concentration lowers the total ionic conductivity. That occurs even when the relative density of the studied ceramics increases with the excess of Li source content. To discuss the possible reasons for such observation, it is worth considering the microstructure and phase purity of LTPO ceramics. From XRD studies, it may be noticed that the introduction of an excess of Li source does not compensate for the lithium loss during heat treatment. Instead, it leads to the formation of secondary phases like $LiTa_3O_8$, appearance of which was also confirmed by EDX studies. ^{31}P MAS NMR spectra showed that besides the above mentioned phase, another unwanted one, Li_3PO_4, may also be formed. Therefore, it may be concluded that the material consists of several impurity phases that affect the transport of Li ions between the grains. However, the most crucial information may be obtained from the SEM images. First of all, the secondary phases, like $LiTa_3O_8$ and Li_3PO_4 are also present in the material without excess of Li source. Although, their content is different in materials with or without an excess of Li_2CO_3 substrate. For the ceramics without the excess of Li source, SEM images reveal very small white areas (ca. 200 nm), assigned to $LiTa_3O_8$ phase, but also some larger ones ascribed to Li_3PO_4 phase. Finally, the analysis of the porosity, grain shape, size distribution and arrangement of secondary phases can be relevant. In samples without Li excess, the pore concentration is higher, but the area of the triple boundary regions is lower than for the sample with 15 wt% excess of Li source. For the three grains that adhere to each other, the more extensive contact area the more conduction paths for Li ions between grains may be formed. Increasing the triple boundary area may hinder the transport of lithium ions. Therefore, we assume that secondary phase concentration, porosity and arrangement of the grains may play a crucial role in lowering the total ionic conductivity for the samples with the excess of Li source. Nonetheless, further studies of this novel compound are required to have deeper insight into the processes that can lead to the improvement of the total ionic conductivity, especially towards the one reported in [32].

4. Conclusions

In this work, the impact of an excess of Li source on the structural and electrical properties of $LiTa_2PO_8$ ceramics, a novel candidate for solid electrolyte in all–solid–state lithium–ion batteries, was investigated. The highest value of the total ionic conductivity σ_{tot} equal to 4.5×10^{-4} S•cm^{-1} at room temperature was obtained for the sample without any excess of Li source. The increment of the Li concentration above the stoichiometric one, results in lowering the total ionic conductivity. The reason for such a decrease may be related to the microstructure and phase purity. Namely, a higher concentration of secondary phases formed during the sintering of the material, porosity, but also arrangement of the neighbouring grains may be responsible for lowering total ionic conductivity in the case of ceramics with the excess of Li source. As for the intrinsic electrical properties of LTPO, we believe that Li(3) site plays a crucial role in high bulk conductivity. The occupation of Li(1) or Li(2) sites is relatively high with regards to Li(3). However, the position of the Li(3) site interconnects the remaining two, providing conduction channels for lithium ions. Generally, good ionic properties of the $LiTa_2PO_8$ sample without excess of Li source make this compound a suitable candidate for solid electrolyte in all solid lithium–ion battery technology. It is hoped that this work will stimulate further research in the field of electrical properties of LTPO.

Declaration of Competing Interest

The authors declare that they have no known competing financial interests or personal relationships that could have appeared to influence the work reported in this paper.

Acknowledgments

The Polish group has received funding from "International Scholarship Exchange of Doctoral Students and Academic Staff" implemented as part of the Activity specified in the application for co-financing of the project no. POWR.03.03.00–00-PN13 / 18 and the National Science Centre, MINIATURA 5, 2021/05/X/ST5/00530. The Spanish group has received funding from the MINECO MAT2016–78362-C4–2R, PID2019–106662RB-C42 projects.

Appendix A. Supporting information

Supplementary data associated with this article can be found in the online version at doi:10.1016/j.jeurceramsoc.2023.05.013.

References

[1] Y. Ding, Z.P. Cano, A. Yu, J. Lu, Z. Chen, Automotive Li-Ion batteries: current status and future perspectives, Electrochem. Energy Rev. 2 (2019) 1–28, https://doi.org/10.1007/s41918-018-0022-z.

[2] A. Paolella, W. Zhu, D. Campanella, S. Kaboli, Z. Feng, A. Vijh, NASICON lithium ions conductors: materials, composites and batteries, Curr. Opin. Electrochem. (2022), 101108, https://doi.org/10.1016/j.coelec.2022.101108.

[3] S. Kundu, A. Kraytsberg, Y. Ein, Recent development in the field of ceramics solid - state electrolytes: I — oxide ceramic solid - state electrolytes, J. Solid State Electrochem (2022) 1809–1838, https://doi.org/10.1007/s10008-022-05206-x.

[4] K. Yang, L. Chen, J. Ma, Y. He, F. Kang, Progress and perspective of Li$_{1+x}$Al$_x$Ti$_{2-x}$(PO$_4$)$_3$ ceramic electrolyte in lithium batteries, InfoMat 3 (2021) 1195–1217, https://doi.org/10.1002/inf2.12222.

[5] Y.Y. Lin, A.X. Bin Yong, W.J. Gustafson, C.N. Reedy, E. Ertekin, J.A. Krogstad, N. H. Perry, Toward design of cation transport in solid-state battery electrolytes: structure-dynamics relationships, Curr. Opin. Solid State Mater. Sci. 24 (2020), 100875, https://doi.org/10.1016/j.cossms.2020.100875.

[6] M.V. Reddy, C.M. Julien, A. Mauger, K. Zaghib, Sulfide and oxide inorganic solid electrolytes for all-solid-state li batteries: a review, Nanomaterials 10 (2020) 1–80, https://doi.org/10.3390/nano10081606.

[7] B. Zhang, R. Tan, L. Yang, J. Zheng, K. Zhang, S. Mo, Z. Lin, F. Pan, Mechanisms and properties of ion-transport in inorganic solid electrolytes, Energy Storage Mater. 10 (2018) 139–159, https://doi.org/10.1016/j.ensm.2017.08.015.

[8] F. Zheng, M. Kotobuki, S. Song, M.O. Lai, L. Lu, Review on solid electrolytes for all-solid-state lithium-ion batteries, J. Power Sources 389 (2018) 198–213, https://doi.org/10.1016/j.jpowsour.2018.04.022.

[9] H. Tsukasaki, H. Morimoto, S. Mori, Ionic conductivity and thermal stability of Li$_2$O–Li$_2$S–P$_2$S$_5$ oxysulfide glass, Solid State Ion. 347 (2020), https://doi.org/10.1016/j.ssi.2020.115267.

[10] X. Lu, X. Li, M. Duan, J. Hai, S. Liu, Preparation of hybrid perovskite-type Li$_{0.33}$La$_{0.56}$TiO$_3$ by adding ionic liquids, J. Rare Earths. (2022) 3–8, https://doi.org/10.1016/j.jre.2022.05.003.

[11] K. Yu, Y. Tian, R. Gu, L. Jin, R. Ma, H. Sun, Y. Xu, Z. Xu, X. Wei, Ionic conduction, colossal permittivity and dielectric relaxation behavior of solid electrolyte Li$_{3x}$La$_{2/3-x}$TiO$_3$ ceramics, J. Eur. Ceram. Soc. 38 (2018) 4483–4487, https://doi.org/10.1016/j.jeurceramsoc.2018.05.023.

[12] R. Gu, J. Kang, X. Guo, J. Li, K. Yu, R. Ma, Z. Xu, L. Jin, X. Wei, Microstructure and ionic conductivity of Li$_{0.5-x}$La$_{0.5}$(Ti$_{1-x}$Nb$_x$)O$_3$ solid-state electrolytes, J. Alloy. Compd. 896 (2022) 1–7, https://doi.org/10.1016/j.jallcom.2021.163084.

[13] E.A. Il'ina, S.V. Pershina, B.D. Antonov, A.A. Pankratov, E.G. Vovkotrub, The influence of the glass additive Li$_2$O-B$_2$O$_3$-SiO$_2$ on the phase composition, conductivity, and microstructure of the Li$_7$La$_3$Zr$_2$O$_{12}$, J. Alloy. Compd. 765 (2018) 841–847, https://doi.org/10.1016/j.jallcom.2018.06.154.

[14] M. Koishi, M. Kotobuki, Preparation of Y-doped Li$_7$La$_3$Zr$_2$O$_{12}$ by co-precipitation method, Ion. (Kiel.) 28 (2022) 2065–2072, https://doi.org/10.1007/s11581-022-04489-4.

[15] S. Song, M. Kotobuki, F. Zheng, C. Xu, Y. Wang, W.D.Z. Li, N. Hu, L. Lu, Roles of Alkaline Earth Ions in Garnet-Type Superionic Conductors, ChemElectroChem 4 (2017) 266–271, https://doi.org/10.1002/celc.201600639.

[16] X. Lu, R. Wang, F. Zhang, J. Li, The influence of phosphorous source on the properties of NASICON lithium-ion conductor Li$_{1.3}$Al$_{0.3}$Ti$_{1.7}$(PO$_4$)$_3$, Solid State Ion. 354 (2020), 115417, https://doi.org/10.1016/j.ssi.2020.115417.

[17] K. Kwatek, J.L. Nowiński, The lithium-ion-conducting ceramic composite based on LiTi$_2$(PO$_4$)$_3$ with addition of LiF, Ion. (Kiel.) 25 (2019) 41–50, https://doi.org/10.1007/s11581-018-2584-5.

[18] K. Kwatek, W. Ślubowska, J.L. Nowiński, A.T. Krawczyńska, I. Sobrados, J. Sanz, Electrical and structural properties of Li$_{1.3}$Al$_{0.3}$Ti$_{1.7}$(PO$_4$)$_3$—based ceramics prepared with the addition of Li$_4$SiO$_4$, Mater. (Basel) 14 (2021) 5729.

[19] G. Kaur, M.D. Singh, S.C. Sivasubramanian, A. Dalvi, Investigations on enhanced ionic conduction in ionic liquid dispersed sol-gel derived LiTi$_2$(PO$_4$)$_3$, Mater. Res. Bull. 145 (2022), 111555, https://doi.org/10.1016/j.materresbull.2021.111555.

[20] S. Martínez-Chaparro, S. Kobylianska, I. Sobrados, R. Jiménez, J. Sanz, Enhanced "overall" ionic conductivity in Li$_{1+x}$Al$_x$Ti$_{2-x}$(PO$_4$)$_3$ ($0.3 \le x \le 0.7$) ceramics prepared from sol-gel powders by spark plasma sintering, J. Eur. Ceram. Soc. 42 (2022) 4248–4258, https://doi.org/10.1016/j.jeurceramsoc.2022.04.009.

[21] J. Zhu, Y. Xiang, J. Zhao, H. Wang, Y. Li, B. Zheng, H. He, Z. Zhang, J. Huang, Y. Yang, Insights into the local structure, microstructure and ionic conductivity of silicon doped NASICON-type solid electrolyte Li$_{1.3}$Al$_{0.3}$Ti$_{1.7}$P$_3$O$_{12}$, Energy Storage Mater. 44 (2022) 190–196, https://doi.org/10.1016/j.ensm.2021.10.003.

[22] T. Okumura, S. Taminato, T. Takeuchi, H. Kobayashi, Minimizing the grain boundary resistance of Li-ion-conducting oxide electrolyte by controlling liquid-phase formation during sintering, ACS Appl. Energy Mater. 1 (2018) 6303–6311, https://doi.org/10.1021/acsaem.8b01278.

[23] G. Zhao, K. Suzuki, T. Seki, X. Sun, M. Hirayama, R. Kanno, High lithium ionic conductivity of γ-Li$_3$PO$_4$-type solid electrolytes in Li$_4$GeO$_4$−Li$_4$SiO$_4$−Li$_3$VO$_4$ quasi-ternary system, J. Solid State Chem. 292 (2020), 121651, https://doi.org/10.1016/j.jssc.2020.121651.

[24] Y. Yang, J. Han, M. DeVita, S.S. Lee, J.C. Kim, Lithium and chlorine-rich preparation of mechanochemically activated antiperovskite composites for solid-state batteries, Front. Chem. 8 (2020) 3–9, https://doi.org/10.3389/fchem.2020.562549.

[25] A. Koedtruad, M.A. Patino, N. Ichikawa, D. Kan, Y. Shimakawa, Crystal structures and ionic conductivity in Li$_2$OHX (X = Cl, Br) antiperovskites, J. Solid State Chem. 286 (2020), 121263, https://doi.org/10.1016/j.jssc.2020.121263.

[26] J. Kim, J. Kim, M. Avdeev, H. Yun, S.J. Kim, LiTa$_2$PO$_8$: a fast lithium-ion conductor with new framework structure, J. Mater. Chem. A. 6 (2018) 22478–22482, https://doi.org/10.1039/c8ta09170f.

[27] N. Ishigaki, K. Kataoka, D. Morikawa, M. Terauchi, K. Hayamizu, J. Akimoto, Structural and Li-ion diffusion properties of lithium tantalum phosphate LiTa$_2$PO$_8$, Solid State Ion. 351 (2020), 115314, https://doi.org/10.1016/j.ssi.2020.115314.

[28] B. Huang, B. Xu, J. Zhang, Z. Li, Z. Huang, Y. Li, C.A. Wang, Li-ion conductivity and stability of hot-pressed LiTa$_2$PO$_8$ solid electrolyte for all-solid-state batteries, J. Mater. Sci. 56 (2021) 2425–2434, https://doi.org/10.1007/s10853-020-05324-9.

[29] Q. Zhang, F. Meng, R. Liao, L. Chen, M. Xu, S. Zhong, J. Chen, A. Lu, Excess Li$_2$O additives to promote grain boundary growth and improve ionic conductivity of LiTa$_2$PO$_8$ solid electrolytes, Front. Mater. 8 (2021) 1–8, https://doi.org/10.3389/fmats.2021.670754.

[30] R. Kim, L.J. Miara, J.-H. Kim, J.-S. Kim, D. Im, Y. Wang, Computational design and experimental synthesis of air-stable solid-state ionic conductors with high conductivity, Chem. Mater. 33 (2021) 6909–6917, https://doi.org/10.1021/acs.chemmater.1c01837.

[31] J. Kim, J. Ha, F. Khefif, J.Y. Kim, J.H. Pee, S.J. Kim, Polymorphism and sodium-ion conductivity of NaTa$_2$PO$_8$ synthesized via the Li$^+$/Na$^+$ ion-exchange reaction of LiTa$_2$PO$_8$, Ceram. Int. 48 (2022) 20712–20720, https://doi.org/10.1016/j.ceramint.2022.04.052.

[32] F. Hussain, P. Li, Z. Li, Theoretical insights into Li-Ion transport in LiTa$_2$PO$_8$, J. Phys. Chem. C. 123 (2019) 19282–19287, https://doi.org/10.1021/acs.jpcc.9b03313.

[33] D. Massiot, F. Fayon, M. Capron, I. King, S. Le Calve, B. Alonso, J. Durand, B. Bujoli, Z. Gan, G. Hoatson, Modelling one- and two-dimensional solid-state NMR, Magn. Reson. Chem. 40 (2002) 70–76, https://doi.org/10.1002/mrc.984.

[34] T.K. Pietrzak, Multi-device software for impedance spectroscopy measurements with stabilization in low and high temperature ranges working under linux environment, Ion. (Kiel.) 25 (2019) 2445–2452, https://doi.org/10.1007/s11581-019-02950-5.

[35] K. Kwatek, W. Ślubowska, J. Trébosc, O. Lafon, J.L. Nowiński, Impact of Li$_{2.9}$B$_{0.9}$S$_{0.1}$O$_{3.1}$ glass additive on the structure and electrical properties of the LATP-based ceramics, J. Alloy. Compd. 820 (2020) 1–10, https://doi.org/10.1016/j.jallcom.2019.153072.

[36] Y. Deng, C. Eames, J.-N. Chotard, F. Lalère, V. Seznec, S. Emge, O. Pecher, C. P. Grey, C. Masquelier, M.S. Islam, Structural and mechanistic insights into fast lithium-ion conduction in Li$_4$SiO$_4$–Li$_3$PO$_4$ solid electrolytes, J. Am. Chem. Soc. 137 (2015) 9136–9145, https://doi.org/10.1021/jacs.5b04444.

[37] J. Emery, T. Šalkus, A. Abramova, M. Barré, A.F. Orliukas, NMR investigations in Li$_{1.3}$Al$_{0.3}$Ti$_{1.7}$(PO$_4$)$_3$ ceramics. Part I: structural aspect, J. Phys. Chem. C. 120 (2016) 26173–26186, https://doi.org/10.1021/acs.jpcc.6b06764.

[38] J. Emery, T. Šalkus, M. Barré, NMR investigations in Li$_{1.3}$Al$_{0.3}$Ti$_{1.7}$(PO$_4$)$_3$ ceramics part iii: local dynamical aspect seen from aluminum and phosphorus sites, J. Phys. Chem. C. 121 (2017) 246–254, https://doi.org/10.1021/acs.jpcc.6b11712.

[39] V. Diez-Gómez, K. Arbi, J. Sanz, Modeling Ti/Ge distribution in LiTi$_{2-x}$Ge$_x$(PO$_4$)$_3$ NASICON Series by ^{31}P MAS NMR and first-principles DFT calculations, J. Am. Chem. Soc. 138 (2016) 9479–9486, https://doi.org/10.1021/jacs.6b03583.

[40] A. Boukhris, T. Ben Hamed, B. Glorieux, M. Ben Amara, Structural study, ^{31}P NMR and europium photoluminescence properties of a new synthetic fillowite-type phosphate: Na$_3$SrMg$_{11}$(PO$_4$)$_9$, Solid State Sci. 67 (2017) 19–29, https://doi.org/10.1016/j.solidstatesciences.2017.03.007.

[41] I.L. Mudrakovskii, V.P. Shmachkova, N.S. Kotsarenko, V.M. Mastikhin, 31P NMR study of I-IV group polycrystalline phosphates, J. Phys. Chem. Solids 47 (1986) 335–339, https://doi.org/10.1016/0022-3697(86)90022-3.

[42] R.K. Brow, C.C. Phifer, G.L. Turner, R.J. Kirkpatrick, Cation effects on ^{31}P MAS NMR chemical shifts of metaphosphate glasses, J. Am. Ceram. Soc. 74 (1991) 1287–1290.

[43] R. Kahlaoui, K. Arbi, I. Sobrados, R. Jimenez, J. Sanz, R. Ternane, Cation miscibility and lithium mobility in NASICON Li$_{1+x}$Ti$_{2-x}$Sc$_x$(PO$_4$)$_3$ ($0<x<0.5$) series: a combined NMR and impedance study, Inorg. Chem. 56 (2017) 1216–1224, https://doi.org/10.1021/acs.inorgchem.6b02274.